

Deformation Patterns and their Stability in Finitely Strained Circular Cell Honeycombs

Christelle Combescure, Ryan Elliott, Nicolas Triantafyllidis

▶ **To cite this version:**

Christelle Combescure, Ryan Elliott, Nicolas Triantafyllidis. Deformation Patterns and their Stability in Finitely Strained Circular Cell Honeycombs. Journal of the Mechanics and Physics of Solids, 2020, 142, pp.103976. 10.1016/j.jmps.2020.103976 . hal-02859820

HAL Id: hal-02859820
https://hal.science/hal-02859820

Submitted on 8 Jun 2020

HAL is a multi-disciplinary open access archive for the deposit and dissemination of scientific research documents, whether they are published or not. The documents may come from teaching and research institutions in France or abroad, or from public or private research centers.

L'archive ouverte pluridisciplinaire **HAL**, est destinée au dépôt et à la diffusion de documents scientifiques de niveau recherche, publiés ou non, émanant des établissements d'enseignement et de recherche français ou étrangers, des laboratoires publics ou privés.

Deformation Patterns and their Stability in Finitely Strained Circular Cell Honeycombs

Christelle Combescure[a], Ryan S. Elliott[b], Nicolas Triantafyllidis[c,d,e,*]

[a] *Laboratoire Modélisation et Simulation Multi-Echelles, Université Paris-Est (UPEM), 77454 Marne-la-Vallée, FRANCE*
[b] *Department of Aerospace Engineering and Mechanics, University of Minnesota, Minneapolis, MN USA 55455*
[c] *Laboratoire de Mécanique des Solides (CNRS UMR 7649), Ecole Polytechnique, Institut Polytechnique de France*
[d] *Département de Mécanique, École Polytechnique, Route de Saclay, Palaiseau 91128, FRANCE*
[e] *Aerospace Engineering Department & Mechanical Engineering Department (emeritus)*
The University of Michigan, Ann Arbor, MI 48109-2140 USA

Abstract

The mechanics of cellular honeycombs—part of the rapidly growing field of architected materials—in addition to its importance for engineering applications has a great theoretical interest due to the complex bifurcation mechanisms leading to failure in these nonlinear structures of high initial symmetry.

Of particular interest to this work are the deformation patterns and their stability of finitely strained circular cell honeycomb. Given the high degree of symmetry of these structures, the introduction of numerical imperfections is inadequate for the study of their behavior past the onset of first bifurcation. Thus, we further develop and explain a group-theoretic approach to investigate their deformation patterns, a consistent and general methodology that systematically finds bifurcated equilibrium orbits and their stability. We consider two different geometric arrangements, hexagonal and square, biaxial compression along loading paths, either aligned or at an angle with respect to the axes of orthotropy, and different constitutive laws for the cell walls which can undergo arbitrarily large rotations, as required by the finite macroscopic strains applied.

We find that the first bifurcation in biaxially loaded hexagonal honeycombs of infinite extent always corresponds to a local mode, which is then followed to find the deformation pattern and its stability. Depending on load path orientation, these first bifurcations can be simple, double or even triple. All bifurcated orbits found are unstable and have a maximum load close to their point of emergence. In contrast, the corresponding instability in square honeycombs always corresponds to a global mode and hence the deformation pattern will depend on specimen size and boundary conditions.

*Corresponding author: nicolas.triantafyllidis@polytechnique.edu

1. Introduction

Honeycomb materials are widely used in industry for their high strength-to-weight ratio and their efficient, shock-absorbing crushing behavior. As such, they have been extensively studied in recent decades, both under static and dynamic loadings, using experimental and numerical techniques. Very recently, especially with the advent of additive manufacturing,"*architected materials*" i.e. materials with complex, periodic microstructures are seeing an impressive growth. Novel architected materials, with intriguing macroscopic properties-by-design, not encountered in natural materials and termed "*metamaterials*", are being introduced at an increasing rate (for the mechanical metamaterials, see the recent review article by Surjadi et al. (2019)). Our work is motivated by the stability and mechanical failure of these important class of engineered materials, due to the complex bifurcation mechanisms of these constitutively and geometrically nonlinear structures of high initial symmetry.

Of the vast literature on the subject, in the interest of space and efficiency only the work relevant to the problem of interest is reported here. Of particular interest to the present investigation is the experimental work of Papka and Kyriakides (1999b,a) which focused attention on the in-plane crushing of circular honeycombs. It was noticed that under this type of loading, honeycombs have a specific crushing mode based on buckling of the cell walls that creates a pattern involving multiple cells. This mechanism was shown to lead to the plateau stress observed on the stress-strain curve of in-plane loaded honeycombs which is followed by densification of the microstructure and stiffening of the material response. There now exists a significant literature of subsequent experimental work studying the static and dynamic behavior of honeycombs, but an exhaustive accounting of this literature is beyond the scope of this presentation.

The early modeling studies focused mainly on hexagonal cell honeycombs, whereas the experiments of Papka and Kyriakides (1999b,a) used circular cell honeycombs. Among these early studies the work of Triantafyllidis and Schraad (1998) and Okumura et al. (2002) on hexagonal cell honeycombs studied various loading directions to determine the onset of buckling. Triantafyllidis and Schraad (1998) focused on double-wall honeycombs with deformation theory of plasticity constitutive behavior in order to compare onsets of plasticity and buckling. Bloch-wave theory was used to compute the onset of buckling and predict the critical wavelength of instability. Okumura et al. (2002) focused on single-wall honeycombs and used a predetermined non-primitive unit-cell based on experimental observations to study microscopic buckling. It was found that under equibiaxial loading microscopic buckling occurs in the form of a third order bifurcation point while under non-equibiaxial loading there is either a simple or a double bifurcation point depending on the orientation of loading. In a separate theoretical study, Saiki et al. (2005) used group theory (symmetry) tools to determine the buckling deformation modes of hexagonal cell honeycomb under in-plane equibiaxial displacement control conditions. In addition to the numerical studies using finite element full-scale modeling, of Papka and Kyriakides (1999b,a), the only other theoretical study of circular cell honeycomb, of which the

authors are aware, is that of Karagiozova and Yu (2008). They focus on strain localization using a structural approach and employ approximate deformation modes based on experimental observations.

In this paper, we perform an extended study of the deformation patterns and their stability for finitely strained circular cell honeycombs. We consider two different geometric arrangements, hexagonal and square, biaxial compression along multiple loading paths, either aligned or at an angle with respect to the axes of orthotropy, and different constitutive laws for the cell walls which can undergo arbitrarily large rotations (Triantafyllidis and Samanta, 1986), as required by the finite macroscopic strains applied. Given the high degree of symmetry of these infinite structures, the introduction of numerical imperfections is inadequate for their study, requiring the use of group theory tools as presented in Combescure et al. (2016). To this end we further develop and explain our group theory-based methodology that systematically finds bifurcating equilibrium paths in these high-symmetry structures.

In Section 2, the problem is defined, the cell wall model is presented along with the general group theoretic method for studying bifurcating equilibrium orbits and their stability in periodic, nonlinear structures of infinite extent. Section 3 outlines the numerical implementation of the cell wall model. Results are presented in Section 4 focusing first on the onset of bifurcation for the three constitutive behaviors and hexagonal honeycombs. Then we determine the primary bifurcating equilibrium orbits for different loading orientations. The section ends with a discussion of the corresponding results for square honeycombs. Conclusions are presented in Section 5.

2. Theory

2.1. Problem Setting

We consider a prismatic structure consisting of circular tubes of initial radius r in two different geometric arrangements—hexagonal and square—with their undeformed, stress-free cross-section shown in Figure 1. Each cylindrical tube deforms only in its cross-sectional plane and is idealized as a curved shell[1] with initial thickness h and unit out-of-plane width. All tubes are rigidly joined together along common generators (perpendicular to the X_1, X_2 plane). Since only 2D deformations of this 3D prismatic structure are considered, for simplicity we refer to it hereafter as a 2D honeycomb consisting of circular cells.

Of interest here is the onset-of-instability surface of the infinite honeycomb, as introduced by Triantafyllidis and Schraad (1998). To this end, a bi-axial far field compression[2] is applied to the honeycomb:

$$\mathbf{\Pi} = -\lambda E \begin{bmatrix} \cos\phi & -\sin\phi \\ \sin\phi & \cos\phi \end{bmatrix} \begin{bmatrix} \cos\theta & 0 \\ 0 & \sin\theta \end{bmatrix} \begin{bmatrix} \cos\phi & \sin\phi \\ -\sin\phi & \cos\phi \end{bmatrix}, \tag{2.1}$$

[1] The thin shell elements ($h \ll 1$) deform only in the X_1, X_2 plane, as shown in Figure 1.

[2] Honeycombs are designed for compression to absorb deformation by cell wall bending; under tension joins come apart.

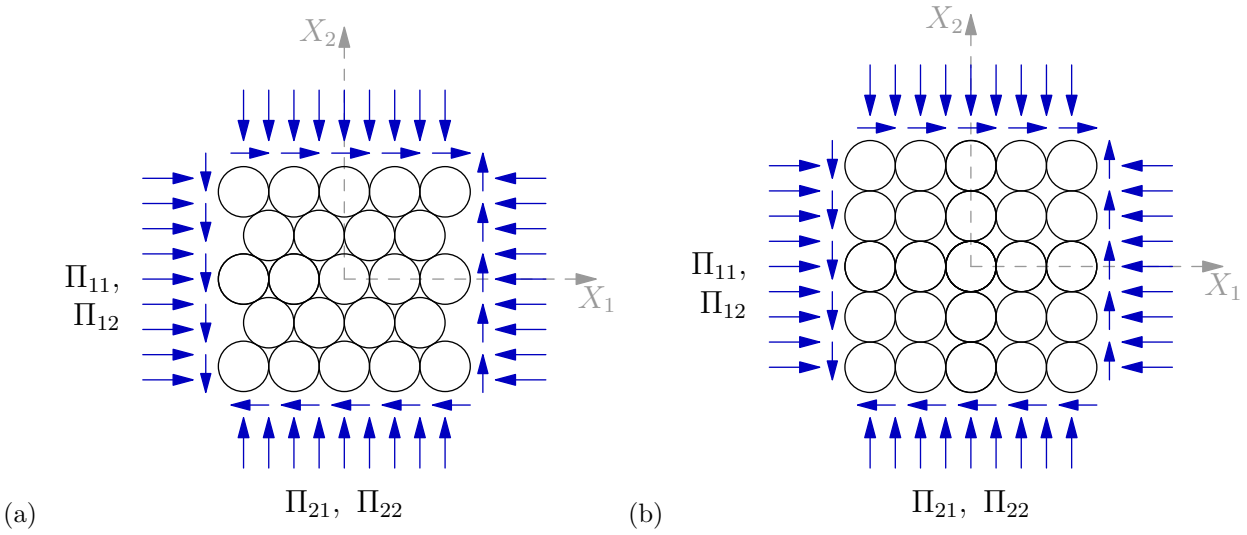


Figure 1: Geometric arrangement and loading of circular (radius r) cell honeycombs: (a) hexagonal and (b) square.

where $\mathbf{\Pi}$ is the applied macroscopic 1st Piola-Kirchhoff stress, $\phi \in [0, \pi/6]$ (for hexagonal honeycombs) or $\phi \in [0, \pi/4]$ (for square honeycombs) is the loading orientation angle, $\theta \in [0, \pi/2]$ is the loading path angle, E is the material's small-strain Young's modulus and $\lambda \geq 0$ is the dimensionless macroscopic (compressive) load parameter.

More specifically, an onset-of-instability surface for the infinite honeycomb is given by the load parameter $\lambda(\theta, \phi)$, corresponding to the first instability encountered along the primary equilibrium path, as a function of the loading path angle θ and the principal stress axes orientation angle ϕ. The influence of material properties on the onset-of-instability surface, as well as the character of the critical bifurcation points and the symmetries and stability of the emerging bifurcated equilibrium orbits are the object of the present investigation.

2.2. Cell Wall Model

Consider a curved wall element of initial length l, thickness h (and unit out-of-plane width) with a cross-section shown in Figure 2. During loading, a material point initially at arc length coordinate s on the curved element's undeformed mid-line (dashed line) moves to a new position on the deformed mid-line by displacements $v(s)$ and $w(s)$ along the local tangential ($\mathbf{t}$) and normal ($\mathbf{n}$) directions, respectively, of the undeformed configuration's mid-line. We adopt the classical Bernoulli-Euler-Navier assumptions where cross-sections normal to the undeformed mid-line remain normal to its deformed counterpart and undergo small strain extension. Consequently, as shown in Figure 2, a material point A at the undeformed (reference) configuration, with initial local coordinates (s, z), moves in the deformed (current) configuration to A'.

A uniaxial plane stress assumption is adopted for the in-plane deformation of the curved wall element

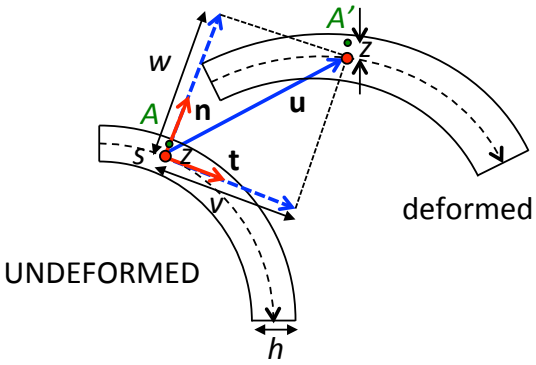


Figure 2: Cell wall kinematics.

with the (small) axial strain in a fiber at distance z from the mid-line $\epsilon_{ss}(s,z) \equiv e(s,z)$ given by:

$$e(s,z) = \varepsilon(s) + z\rho(s) \ , \tag{2.2}$$

where, in view of the finite rotations and axial stretching, the mid-line axial strain $\varepsilon(s)$ and the bending strain $\rho(s)$ are expressed in terms of the normal $v(s)$ and tangential $w(s)$ displacements by:

$$\begin{aligned} \varepsilon &= \left[(1+g)^2 + f^2\right]^{1/2} - 1, \quad f \equiv \frac{dw}{ds} - \kappa v \ , \quad g \equiv \frac{dv}{ds} + \kappa w \ , \\ \rho &= \left[f\frac{dg}{ds} - (1+g)\frac{df}{ds} \right] / \left[(1+g)^2 + f^2\right] - \kappa \ , \end{aligned} \tag{2.3}$$

where $\kappa(s)$ is the curvature of the reference configuration mid-line.

The internal virtual work contribution from a cell wall segment of length l to the weak form of the equilibrium equations is:

$$\delta\mathcal{W}_{int} = \int_0^l (N\delta\varepsilon + M\delta\rho)\, ds \ ; \quad N \equiv \int_{-h/2}^{h/2} \sigma \, dz \ , \ M \equiv \int_{-h/2}^{h/2} \sigma z \, dz \ , \tag{2.4}$$

where $N(s)$ and $M(s)$ are the axial force and bending moment resultants, respectively, and $\sigma_{ss}(s,z) \equiv \sigma(s,z)$ is the normal axial stress in the cell wall, work-conjugate to $e(s,z)$ defined in (2.2). The Euler-Lagrange equations corresponding to (2.2)–(2.4) can be shown to coincide with the exact equilibrium equations of this element in the current configuration, thus making this structural theory a consistent one (the interested reader is referred to Triantafyllidis and Samanta, 1986, for a detailed discussion).

For the case of an elastic material, or a deformation theory of plasticity model[3] (as in the present case of uniaxial stressing of metallic structures in the absence of unloading), one can find an energy density of the

[3]Due to the high tangent moduli—upon a sudden change of loading path—in some incremental plasticity theories, the so-called "*deformation theory*" plasticity models, derived by integrating the constitutive response along proportional loading paths are a preferred alternative for stability calculations in elastoplastic structures. The present case of uniaxial stressing of the cell walls does result in such a model in the absence of unloading. For a detailed discussion of the use of deformation theories of plasticity in stability calculations, the interested reader is referred to the review article by Hutchinson (1974).

curved wall $\widehat{w}$ (per unit volume) and by integrating it through the thickness (for a wall of unit out-of-plane width) obtain an energy density per unit length W:

$$\widehat{w}(e) = \int_0^e \sigma(e')de' \ , \quad W(\varepsilon, \rho) = \int_{-h/2}^{h/2} \widehat{w}(\varepsilon + z\rho)dz \ . \tag{2.5}$$

Consequently, the contribution of internal virtual work from each cell wall section of length l is the first variation of the cell wall's stored elastic energy $\mathcal{E}_{cell}$:

$$\begin{gathered}\delta\mathcal{W}_{int} = \delta\mathcal{E}_{cell} = \int_0^l \left[\frac{\partial W}{\partial \varepsilon}\delta\varepsilon + \frac{\partial W}{\partial \rho}\delta\rho\right] ds \ ; \quad \left(\mathcal{E}_{cell} = \int_0^l W ds\right) \ , \\ N = \frac{\partial W}{\partial \varepsilon} = \int_{-h/2}^{h/2} \frac{\partial \widehat{w}}{\partial e}\, dz \ , \ M = \frac{\partial W}{\partial \rho} = \int_{-h/2}^{h/2} \frac{\partial \widehat{w}}{\partial e} z\, dz \ ; \ \left(\sigma = \frac{\partial \widehat{w}}{\partial e}\right) \ .\end{gathered} \tag{2.6}$$

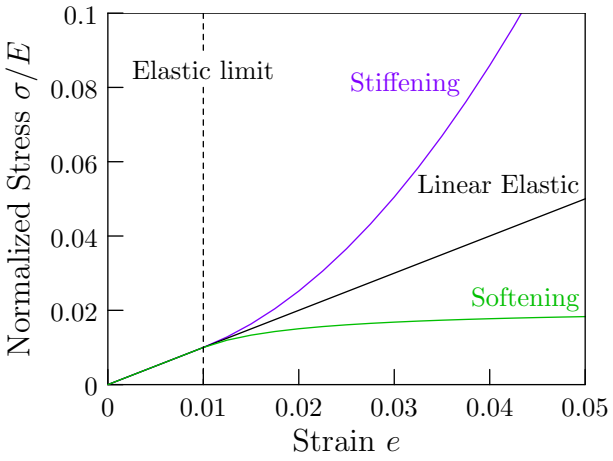


Figure 3: Uniaxial response of cell walls: a linearly elastic response ($m = 1$), a stiffening response ($m = 2 > 1$) – corresponding to elastomeric cell walls – and a softening response ($m = 0.9 < 1$) – typical of metallic or some polymeric cell walls.

A piecewise power law response (relating σ to e), common in applications involving the stability of elastoplastic structures (e.g. Hutchinson (1974)), with the following energy density is adopted :

$$\widehat{w}(e) = E(\varepsilon_l)^2\left[\frac{1}{\eta(1+\eta)}\left(\frac{|e|}{\varepsilon_l}\right)^{\eta+1} + \frac{\eta-1}{\eta}\frac{|e|}{\varepsilon_l} - \frac{\eta}{1+\eta} + \frac{1}{2}\right] \ , \quad \begin{cases} \eta = 1 \text{ for } |e| \le \varepsilon_l \ , \\ \\ \eta = m \text{ for } |e| > \varepsilon_l \ , \end{cases} \tag{2.7}$$

where E is the material's small-strain Young modulus and ε_l its linear elastic limit under uniaxial loading.

Three different cases will be investigated: a linearly elastic response ($m = 1$), a stiffening response ($m > 1$) – typical of elastomeric cell walls – and a softening response ($m < 1$) – typical of metallic or some polymeric cell walls. The corresponding representative dimensionless stress-strain curves are plotted (using $\varepsilon_l = 0.01$) in Figure 3.

2.3. Group Theory Approach

The energy of the structure is thus the sum of the energies of each cell. Assuming rigid joints, i.e. that cells are welded to their neighbors at their contact points, the displacements and rotations of each joint are the same for the two cells sharing it:

$$\mathcal{E}(u;\lambda) = \sum_{I=1}^{N_{tot}} \int_0^{2\pi r} W_I(\varepsilon,\rho)ds - \Pi_{ij}^B\,(U_{ij}-\delta_{ij})A_{domain}\;, \quad u\in H\;, \quad \lambda\geq 0\;, \tag{2.8}$$

where W_I, the energy density of cell I, is defined in (2.5), the macroscopic Biot stress components $\Pi_{ij}^B(=\Pi_{ij})$ are given in (2.1), $U_{ij}(=F_{ij})$ are the components of the macroscopic right stretch tensor[4] and A_{domain} is the area of the computational domain. Since only biaxial compression is considered, the load parameter is positive $\lambda\geq 0$, according to (2.1). Moreover, the unknown $u\equiv(\mathbf{U};v_I(s),w_I(s)),\ I=1,N_{tot}$ consists of the macroscopic stretch tensor plus the local displacement fields of all cells, which must satisfy the displacement and slope continuity conditions at all contact points. The functional space of all admissible fields u is denoted by H. To avoid issues associated with domains of infinite extent, we consider arbitrarily large—but finite—domains of dimensions $L_1\times L_2$ with N_{tot} cells and appropriate periodicity conditions at the opposite boundaries of the chosen domain.

The fundamental concept used to study the bifurcated equilibrium paths and their stability in any conservative elastic system with symmetries is the existence of a group G of transformations that leave its energy $\mathcal{E}(u;\lambda)$—defined in (2.8) for the problem at hand—unchanged, i.e., invariant under the action of all transformations $g\in G$. More specifically, to each element $g\in G$ we associate a transformation T_g (termed "*representation*" of g) acting on $u\in H$ with image $T_g[u]\in H$ that satisfies

$$\mathcal{E}(u;\lambda) = \mathcal{E}(T_g[u];\lambda)\,; \quad \forall\lambda\geq 0\,,\ \forall u\in H\,,\ \forall g\in G\,. \tag{2.9}$$

It follows from (2.9) that the variation of $\mathcal{E}$ with respect to its argument u ($\delta\mathcal{E}=\mathcal{E}_{,u}\delta u$, where $\mathcal{E}_{,u}$ is the first order functional derivative of $\mathcal{E}$ with respect to u, a linear operator acting on $\delta u\in H$) has the property of "*equivariance*"[5]

$$T_g[\mathcal{E}_{,u}(u;\lambda)]\delta u = \mathcal{E}_{,u}(T_g[u];\lambda)\delta u\,; \quad \forall\lambda\geq 0\,,\ \forall u,\delta u\in H\,,\ \forall g\in G\,. \tag{2.10}$$

The system's equilibrium solutions u are found by extremizing its energy. Consequently all solutions of the system $\mathcal{E}_{,u}(u;\lambda)\delta u=0$ must satisfy (2.10). It is more appropriate to talk about *orbits* of equilibrium

[4] Macroscopic rotation is ignored as superfluous i.e. $\mathbf{F}=\mathbf{U}$, since the stress state can be rotated with respect to the axes of orthotropy of the honeycomb. The corresponding work conjugate stress measure is the (symmetric) Biot stress $\mathbf{\Pi}^B$, which in this special case equals the 1st Piola-Kirchhoff stress $\mathbf{\Pi}$ given in (2.1).

[5] Assuming orthogonality of the representation operator $(T_g)^{-1}=(T_g)^t$, a property satisfied in most applications in mechanics and true for all finite groups G, as will be the case of the discretized problems considered here.

paths, since in view of the equivariance described in (2.10), applying to an equilibrium solution u the transformation T_g automatically generates another equilibrium solution $T_g[u]$.

A subset of these equilibrium solutions, termed "*principal solutions*" and denoted by $\overset{0}{u}(\lambda)$, are invariant under all transformations T_g. These solutions belong to an invariant subspace of H, denoted $\mathcal{S}_G$ and termed the "*fixed-point space*"

$$\mathcal{E}_{,u}(\overset{0}{u}(\lambda);\lambda)\delta u = 0 \ , \ \forall \lambda \geq 0 \ ; \quad \overset{0}{u} \in \mathcal{S}_G \equiv \{u \in H |\ T_g[u] = u \ , \ \forall g \in G\} \ . \tag{2.11}$$

To determine the stability of a principal solution, one has to check the positive definiteness of the self-adjoint bilinear operator $\mathcal{E}^0_{,uu}$, evaluated on the principal path $\overset{0}{u}(\lambda)$, by finding its eigenvalues $\beta(\lambda)$

$$(\mathcal{E}^0_{,uu}\Delta u)\delta u = \beta(\lambda) < \Delta u, \delta u > \ ; \quad \forall \delta u \in H \ ; \ \mathcal{E}^0_{,uu} \equiv \mathcal{E}_{,uu}(\overset{0}{u}(\lambda);\lambda) \ , \tag{2.12}$$

where Δu is the corresponding eigenvector and $< \cdot \ , \ \cdot >$ denotes an inner product in H. A stable solution corresponds to the case where the minimum eigenvalue is positive, $\beta_{min} > 0$. For a well-posed problem, the stress-free (unloaded) configuration at $\lambda = 0$ is stable. As the load increases stability will be lost at the first bifurcation point encountered along the loading path parameterized by λ.

It can be shown, e.g., Golublitsky et al. (1988); McWeeny (2002), that i) associated with the representation T of G, there exists a symmetry-adapted basis of H with respect to which the operator $\mathcal{E}^0_{,uu}$ defined in (2.12) is block-diagonalized, and ii) the space of admissible functions H can be uniquely decomposed (*isotypic decomposition*) into a direct sum, $H = \oplus_{\mu=1}^{\eta} V^\mu$, of mutually orthogonal invariant subspaces V^μ (η being the number of conjugacy classes of G). Each subspace V^μ is associated to a n_μ-dimensional irreducible representation τ^μ of G, also termed "*irrep*", from which an appropriate projection operator can be constructed that gives the V^μ component of any function of the admissible space H.

Bifurcation points along the principal equilibrium path are characterized by a critical load λ_b, for which there exist zero eigenvalues of the operator $\mathcal{E}^0_{,uu}$ (i.e. $\beta(\lambda_b) = 0$)

$$(\mathcal{E}^b_{,uu}\overset{i}{u})\delta u = 0 \ , \ \overset{i}{u} \in \mathcal{N}_\mu \ , \ < \overset{i}{u}, \overset{j}{u} >= \delta_{ij} \ , \ i,j = 1,\ldots,n_\mu \ ; \ \forall \delta u \in H \ ; \ \mathcal{E}^b_{,uu} \equiv \mathcal{E}_{,uu}(\overset{0}{u}(\lambda_b);\lambda_b) \ , \tag{2.13}$$

where the eigenmodes $\overset{i}{u}$ form an orthonormal basis[6] of $\mathcal{N}_\mu$, the n_μ-dimensional null space of the operator $\mathcal{E}^b_{,uu}$. Some additional conditions must also hold to ensure that λ_b is a bifurcation and not a limit (i.e. turning) point, as follows

$$\mathcal{E}^b_{,u\lambda}\overset{i}{u} = 0 \ ; \quad i = 1,\ldots,n_\mu \ . \tag{2.14}$$

[6] In some cases it is convenient to use an alternative normalization of the basis for $\mathcal{N}_\mu$. In particular for the Lyapunov-Schmidt-Koiter asymptotic analysis discussed later in this section, it is convenient to normalize according to the conditions $< \overset{i}{u}, \overset{j}{u} >= \chi\delta_{ij}$, where χ is determined by the condition $\mathcal{E}_{ij\lambda} = -\delta_{ij}$. The coefficient $\mathcal{E}_{ij\lambda}$ is discussed after Eq. (2.21) and defined in Triantafyllidis and Peek (1992).

For such points, equilibrium paths (termed *primary paths*) cross, or bifurcate, from the principal path. It can be shown that the null space $\mathcal{N}_\mu$ of the stability operator $\mathcal{E}^b_{,uu}$ is an invariant subspace of V^μ, i.e. $\mathcal{N}_\mu \subseteq V^\mu$, associated with the irreducible representation τ^μ of dimension n_μ.

For the case of periodic structures, i.e. groups having translational symmetries (in addition to point symmetries), one can find $\overset{0}{u}$ by solving the equilibrium equations on a "*primitive cell*", which is the smallest unit cell of dimensions $l_1 \times l_2$ (for 2D honeycombs) that by translation along different coordinate directions (not necessarily orthogonal to each other, depending on the honeycomb's point group symmetry) produces the infinite structure. Moreover, one can take advantage of the Bloch-wave representation theorem, according to which any eigenmode Δu of the stability operator $\mathcal{E}^0_{,uu}$ in (2.12) admits the following representation

$$\Delta u(X_1, X_2) = \exp[i(k_1 X_1 + k_2 X_2)]\; p(X_1, X_2)\;, \tag{2.15}$$

where $i = \sqrt{-1}$ is the imaginary unit, $p(\mathbf{X})$ is a periodic function defined on the primitive unit cell and $\mathbf{k}$ is the wavenumber vector. All admissible values of $\mathbf{k}$ are in the "*Brillouin zone*" $\mathcal{B} \subset [0, 2\pi/l_1) \times [0, 2\pi/l_2)$, defined as a primitive cell of the reciprocal lattice in $\mathbf{k}$ space.

Of interest here is the load λ_b and the associated wavenumber $\mathbf{k}_b$ corresponding to the onset of the first bifurcation encountered along the loading path of interest defined in (2.1). To find this, we proceed as follows: we first determine the minimum eigenvalue of the stability operator $\beta_{min}(\lambda, \mathbf{k})$ for a given pair[7] $(\lambda, \mathbf{k})$ (see definition (2.12))

$$\beta_{min}(\lambda, \mathbf{k}) \equiv \min_{\|\Delta u\|=1} (\mathcal{E}^0_{,uu}\Delta u)\Delta u\;; \quad \forall\; \Delta u(\mathbf{X}, \mathbf{k}) = \exp[i(\mathbf{k}\cdot\mathbf{X})]\; p(\mathbf{X})\;. \tag{2.16}$$

We subsequently find $\lambda_{cr}(\mathbf{k})$, the lowest nontrivial λ root of β_{min} for each fixed $\mathbf{k}$,

$$\beta_{min}(\lambda_{cr}(\mathbf{k}), \mathbf{k}) = 0\;; \quad \beta_{min}(\lambda, \mathbf{k}) > 0\;,\; 0 \le \lambda < \lambda_{cr}(\mathbf{k})\;. \tag{2.17}$$

Finally, the sought bifurcation load λ_b is the infimum[8] of $\lambda_{cr}(\mathbf{k})$ with respect to $\mathbf{k}$. This is computed by scanning all independent wavevectors $\mathbf{k}$, which due to the point group symmetry elements of G lie in a subdomain $\mathcal{B}_G \subset \mathcal{B}$

$$\lambda_b \equiv \inf_{\mathbf{k}\in\mathcal{B}_G} \lambda_{cr}(\mathbf{k})\;. \tag{2.18}$$

Note that the wavenumbers $\mathbf{k}_b$ corresponding to λ_b are not unique. In particular, the existence of an energy implies $\beta_{min}(\lambda; -\mathbf{k}) = \beta_{min}(\lambda; \mathbf{k})$. The critical vectors $\mathbf{k}_b$ allow the identification of a new (larger than the primitive) unit cell required for calculating the equilibrium paths emerging from λ_b (Sorkin et al., 2014).

[7] Due to singular behavior of the Bloch-wave behavior near $\mathbf{k} = \mathbf{0}$, $\beta_{min}(\lambda, \mathbf{0})$ must be defined slightly different from the general case. In particular, the case for which $p(\mathbf{X}) =$ constant must be excluded from consideration.

[8] We consider the inf instead of the min in (2.18) in view of possible singularities of the $\lambda_{cr}(\mathbf{k})$ surface defined on the Brillouin zone, see Triantafyllidis and Schraad (1998).

To avoid introducing superfluous notations, we will denote once more the energy defined on this new (larger than the primitive) unit cell by $\mathcal{E}$ and the corresponding symmetry group (a subgroup of the original) again by G. The corresponding fundamental solution $\overset{0}{u}(\lambda)$ and primitive cell remain the same as in the original problem (on the $L_1 \times L_2$ domain[9]) defined in (2.8).

To compute the (primary) bifurcated paths $\overset{b}{u}(\lambda)$ emerging from $\overset{0}{u}(\lambda)$ at λ_b, the following asymptotic expressions, resulting from the projection of the equilibrium equations into the null space $\mathcal{N}_\mu$ and termed "*Lyapunov-Schmidt-Koiter*" (LSK) asymptotics, are used

$$\lambda = \lambda_b + \lambda_1 \xi + \frac{1}{2}\lambda_2 \xi^2 + \cdots \ , \ \overset{b}{u}(\lambda) = \overset{0}{u}(\lambda) + \xi \sum_{i=1}^{n_\mu} \alpha_i \overset{i}{u} + O(\xi^2) \ , \tag{2.19}$$

where ξ is the path's "*bifurcation amplitude*" parameter and α_i the components of the bifurcated path's unit tangent vector. For the case of an asymmetric bifurcation $\lambda_1 \neq 0$, the tangents α_i are given by the system of n_μ polynomial equations of order two

$$\sum_{j,k=1}^{n_\mu} \alpha_j \alpha_k \mathcal{E}_{ijk} + 2\lambda_1 \sum_{j=1}^{n_\mu} \alpha_j \mathcal{E}_{ij\lambda} = 0 \ , \ \| \boldsymbol{\alpha} \| = 1 \ , \quad i = 1, \ldots, n_\mu. \tag{2.20}$$

For the case of a symmetric bifurcation $\lambda_1 = 0$, $\mathcal{E}_{ijk} = 0$, the tangents α_i are given by the following system of n_μ polynomial equations of order three ($\mathcal{E}_{ijk} = 0$ implies symmetry of solutions $\pm\boldsymbol{\alpha}$)

$$\sum_{j,k,l=1}^{n_\mu} \alpha_j \alpha_k \alpha_l \mathcal{E}_{ijkl} + 3\lambda_2 \sum_{j=1}^{n_\mu} \alpha_j \mathcal{E}_{ij\lambda} = 0 \ , \ \| \boldsymbol{\alpha} \| = 1 \ , \quad i = 1, \ldots, n_\mu. \tag{2.21}$$

In the previous equations, the coefficients $\mathcal{E}_{ijkl}$, $\mathcal{E}_{ijk}$ and $\mathcal{E}_{ij\lambda}$ are expressed in terms of higher order functional derivatives of the energy evaluated at the bifurcation point (Triantafyllidis and Peek (1992)). As mentioned in Footnote 6, it is always possible to normalize these equations so that $\mathcal{E}_{ij\lambda} = -\delta_{ij}$.

The stability operator at λ_b determines the eigenmodes and the corresponding null space $\mathcal{N}^\mu$, which allows for an efficient calculation of the bifurcation asymptotics in (2.19). It turns out that the projection of the bifurcated equilibrium solution on the null space $\mathcal{N}_\mu$ is equivariant[10] with respect to the elements of τ^μ and hence we can find the corresponding symmetry-reduced equivalent set of equations (2.20) or (2.21), leading to the calculation of a unique representative of each distinct equilibrium orbit emerging from λ_b.

An important remark is in order here about the calculation of the equilibrium paths emerging at λ_b. A group-theoretic analysis would entail classifying the maximal isotropy subgroups of the corresponding irreps τ^μ in order to predict what kinds of bifurcations generically occur, without relying on the asymptotic expansions (2.20), (2.21). This general method is preferable to the LSK asymptotics, especially for large n_μ when one may need even higher-order expansions, since $\mathcal{E}_{ijk} = \mathcal{E}_{ijkl} = 0$.

[9] The initial $L_1 \times L_2$ domain of the periodic structure is constructed from the primitive domain $l_1 \times l_2$ by taking $N_1 \times N_2 = N_{tot}$ primitive cells (see also (2.8)).

[10] The equivariance definition for equilibrium equations in subspace $\mathcal{N}_\mu$ is analogous to the general one in (2.10)

Having established the primary bifurcation orbits, we can then calculate their stability and corresponding bifurcation points treating each $\overset{b}{u}(\lambda)$ as a new principal solution $\overset{0}{u}(\lambda)$. The strategy followed is to sequentially apply the above-described procedure to follow each bifurcated equilibrium orbit by identifying every time a new unit cell for the corresponding eigenmodes, the corresponding energy and the new symmetry group. The basic method, called the "*branch-following and bifurcation method*" has been introduced for the case of atomistic bifurcation calculations for shape memory alloys by Elliott et al. (2006), Elliott et al. (2011).

3. Numerical Aspects

The FEM discretization of the curved cell wall model presented in Section 2.2 requires the normal and tangential displacements $v(s)$ and $w(s)$ as well as their first derivatives dv/ds and dw/ds as nodal degrees of freedom, resulting in four d.o.f. per node. As a consequence, Hermitian cubic shape functions are used for interpolation coupled with a numerical integration scheme of four Gauss points per element. This choice of shape functions leads to a small (decreasing with mesh refinement) error in the "*patch test*," since it generates strains upon rigid body motions. Hermitian cubics in s cannot properly represent the functions $\cos(s)$ and $\sin(s)$ entering the expressions for the corresponding tangential and normal displacements. For this reason, the curved shell element presented above is used only in the computation of the principal path and its stability based on a primitive unit cell, with four elements per cell wall segment (circular sector of $\pi/3$ for hexagonal geometry or $\pi/2$ for square geometry). A finer discretization of the cell walls using flat wall elements (simplified version of the curved shell with curvature $\kappa = 0$) is used for larger unit cell computations, since straight elements always satisfy the patch test. Although finer discretizations were used, the calculations presented here are based on six elements per cell wall segment. Finally, for the constitutively nonlinear cell walls, an 81 equidistant points trapezoidal integration rule is employed.

The negligible axial strains in the cell walls result in the additional simplification of common nodal degrees of freedom dv/ds and dw/ds, expressed in their local coordinate system, for all elements sharing this node in a common joint. The finite rotation of the rigid joint is the same for each element ending in the common joint, as shown in Triantafyllidis and Schraad (1998). Consequently, when going from a rotated local coordinate system to a fixed global one, the only degrees of freedom affected are the normal and tangential displacement degrees of freedom, v and w, respectively.

The FEM-discretized system's d.o.f. are the nodal displacements and rotations of the cell walls, denoted by $\widehat{\mathbf{u}}$ plus the components of the right stretch tensor $\mathbf{U}$ and hence the discretization of the displacement field u in (2.8) is $(\mathbf{U}, \widehat{\mathbf{u}})$. The nonlinear equilibrium equations resulting from the FEM discretization of $\mathcal{E}_{,u}\delta u$ are then solved using an incremental Newton-Raphson method, as described in Combescure et al. (2016).

To bypass the difficulty of limit loads in λ, numerical calculations employ its work-conjugate dimensionless displacement Δ (recalling the loading term from (2.8), we define $\Delta \equiv [\Pi_{ji}\ (U_{ij} - \delta_{ij})]/\lambda)$ (see Triantafyllidis

and Schraad (1998)) in combination with arc length continuation methods.

4. Results

Here are presented the results of the FEM calculations for circular cell honeycombs in hexagonal and square array arrangements, submitted to the in-plane stress loadings defined in (2.1). This study addresses the influence of the cell wall material's constitutive nonlinearity, loading angle and path orientation on the in-plane onset-of-instability surface as defined in Section 2.1. For the hexagonal geometry honeycomb, primary bifurcation orbits are presented for three different types of radial loading paths, one for each type of point on the onset-of-instability surface corresponding to different bifurcations with "*local modes*", i.e. eigenmodes with finite wavelengths $\mathbf{k}_b \neq \mathbf{0}$ that are periodic on a finite number of primitive cells. For the square geometry honeycomb, all points on the onset-of-instability surface correspond to "*global modes*", i.e. eigenmodes with (infinite) long wavelengths $\mathbf{k}_b \to \mathbf{0}$, in which case no primary bifurcations are considered since the corresponding equilibrium paths will always depend on boundary conditions of the domain considered.

It should also be pointed out that cell wall contact is not taken into account in the FEM simulations. As a consequence, computations presented hereafter concern paths up to the point where the first contact is encountered, as indicated in the corresponding onset-of-instability curves.

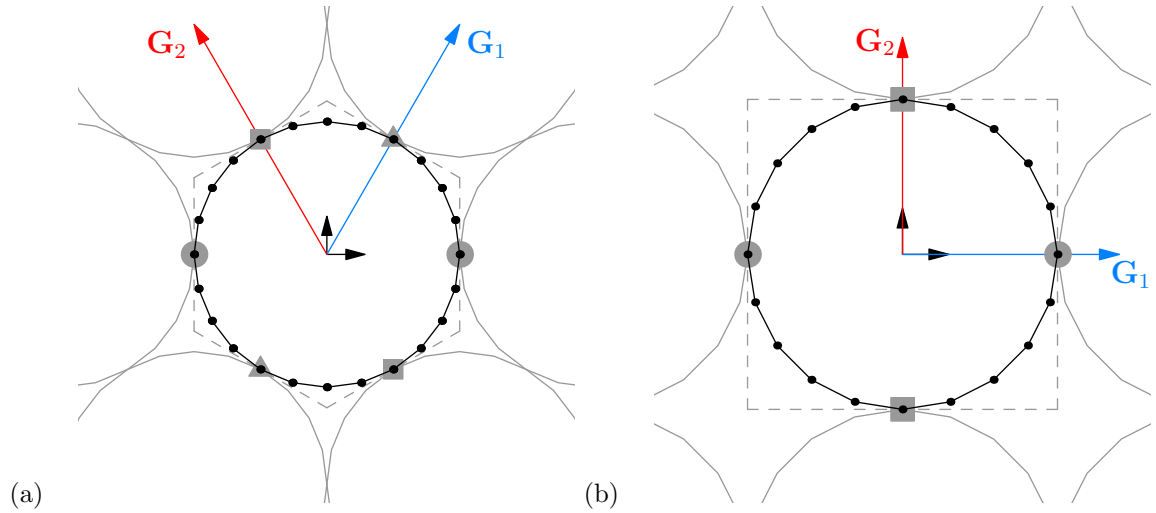


Figure 4: Primitive unit cell used for (a) the hexagonal honeycombs and (b) the square honeycombs. Cell contact points that are coupled in the Bloch-wave calculations are marked identically.

The primitive cell used for the hexagonal honeycomb calculations is depicted in Figure 4(a) and for the square honeycomb calculations is depicted in Figure 4(b). Translations of the primitive cell pattern by $2r$ along the $\mathbf{G}_1$ and $\mathbf{G}_2$ directions give the infinite honeycomb.

Calculating the principal equilibrium solutions $\overset{0}{u}(\lambda, \theta, \phi)$ along a given path with loading orientation ϕ and angle θ (see (2.1)) is based on solving the discretized equilibrium equations $\mathcal{E}_{,u}\delta u = 0$ on this cell, as described in Section 2, subject to periodicity conditions of the joint nodes on opposites faces, as depicted in Figure 4. It should be mentioned at this point that the vector space in which we seek these principal equilibrium solutions is the fixed-point subspace $\mathcal{S}_G$, defined in (2.11).

For a fixed loading orientation ϕ and angle θ, we seek the lowest value of the loading parameter λ at which the infinite honeycomb becomes unstable, as described in Section 2.3. The primitive cell is again involved in the corresponding calculations which use the Bloch-wave representation (2.15) and result in coupled boundary conditions, involving the wavenumber $\mathbf{k}$, between the contact nodes on opposites faces—see Figure 4. Details of the calculations, in particular on the actual domain in the reciprocal $\mathbf{k}$-space used in calculations (for reasons of coding simplicity larger than the irreducible domain of the first Brillouin zone $\mathcal{B}_G$) are similar to those described in Combescure et al. (2016) and need not be elaborated here.

4.1. Material Parameters

In the following, the honeycomb's dimensions, constitutive material's parameters, as well as nonlinear parameters for the power law are given in Table 1. The latter were chosen so that they fit with the experiments in Papka and Kyriakides (1999a) for the case of softening behavior.

Table 1: Cell dimensions and constitutive parameters.

cell radius (mm) r = 3.48	wall thickness (mm) h = 0.144
Young's modulus (MPa) $E = 2500$	linear elastic limit $\varepsilon_l = 10^{-2}$
power law exponent (softening) $m = -0.9$	power law exponent (stiffening) $m = 2.0$

4.2. Hexagonal Honeycombs

4.2.1. Principal Paths and Onset-of-Instability Curves Based on the Primitive Cell

The onset-of-instability curves computed for the loading defined in (2.1), plotted in macroscopic stress space for the circular cell hexagonal honeycomb with different constitutive laws of the cell walls, are shown in Figure 5 to Figure 7. Onset-of-instability curves are plotted in solid lines, curves indicating the onset of cell wall contact are plotted in lines with cross markers, curves indicating a limit (maximum) load are plotted in lines with triangular markers, and curves with dotted lines indicate reaching the elastic limit (onset of nonlinear behavior). Numbers next to the onset of bifurcation curves indicate the order of the corresponding bifurcation point.

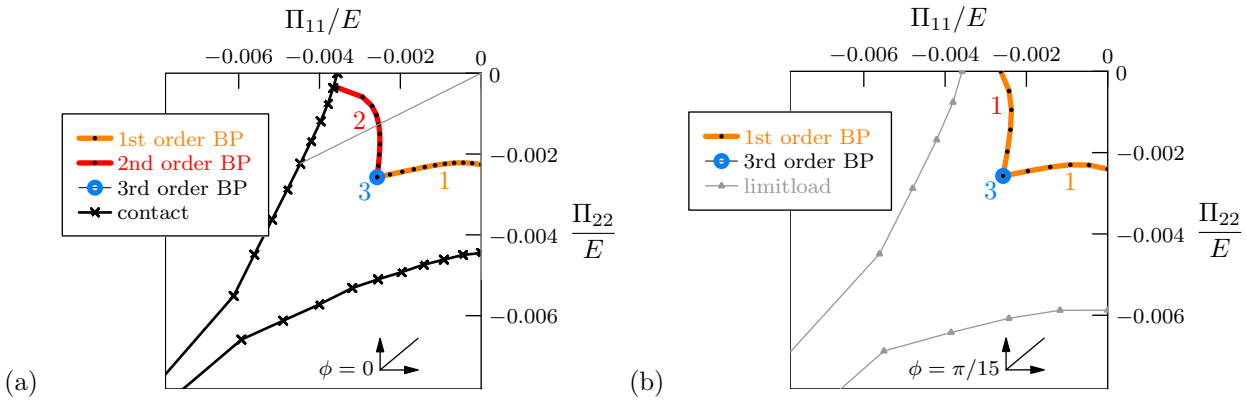


Figure 5: Onset-of-instability (bifurcation) for circular cell hexagonal honeycombs, with linearly elastic cell walls under biaxial in-plane loading (a) aligned with the axes of orthotropy ($\phi = 0$) and (b) rotated with respect to the axes of orthotropy ($\phi = \pi/15$). Note that the rotation of principal loading axes ($\phi \neq 0$) results in reaching a maximum load prior to cell wall contact. The loading paths for which post-bifurcation equilibria are calculated are: $\theta = \tan^{-1}(0.4)$ (plotted in solid, thin grey line), $\theta = \pi/4$ (equibiaxial loading) and $\theta = \pi/2$ (uniaxial compression along X_2).

The onset of bifurcation, along with the first contact and maximum load curves for circular cell hexagonal honeycombs with linearly elastic cell walls are plotted in Figure 5. The graph in Figure 5(a) corresponds to biaxial loading aligned with the axes of orthotropy ($\phi = 0$). Notice that, due to the symmetry of the structure and loading for this case, three possibilities exist for the onset of bifurcation: simple (indicated by number 1) for loading paths $\pi/4 < \theta \leq \pi/2$, double (indicated by number 2) for loading paths $0 \leq \theta < \pi/4$ and triple for the highest symmetry case of the equibiaxial loading path $\theta = \pi/4$. The graph in Figure 5(b) corresponds to biaxial loading rotated with respect to the axes of orthotropy ($\phi = \pi/15$). Due to the lower symmetry of the problem, all points at the onset of bifurcation along each loading path are simple, save for the equibiaxial loading path $\theta = \pi/4$ that is identical to the $\phi = 0$ case and hence has a triple bifurcation point. Note also that the rotation of principal loading axes results in reaching a maximum load prior to cell wall contact for almost all loading paths except a narrow zone around $\theta = \pi/4$.

The onset of bifurcation results for $\phi = 0$ are qualitatively similar with the ones presented for the straight cell wall hexagonal honeycomb by Triantafyllidis and Schraad (1998) and Okumura et al. (2002). Along each loading path, contact occurs before a maximum load is reached. No bifurcation is observed for the case of nearly uniaxial compression along X_1, i.e. for $|\theta| \ll 1$, until first contact is detected. For the highest symmetry case of equibiaxial compression, no cell wall contact is detected, even for loads several times higher than the one corresponding to first bifurcation. Similarly to what was noted by Okumura et al. (2002), for biaxial loading aligned with the axes of orthotropy, the paths where $|\Pi_{11}| > |\Pi_{22}|$ have bifurcation points of order two (two eigenmodes) whereas the paths where $|\Pi_{11}| < |\Pi_{22}|$ have simple bifurcation points (one eigenmode). As for the equibiaxial compression, it is the only loading path with a triple bifurcation, due to its highest symmetry. These results will be explained by the Bloch-wave calculations which give the wave

vectors $\mathbf{k}_b$ corresponding to the critical load and the symmetry group of the energy defined on the domain required for the post-bifurcated orbit.

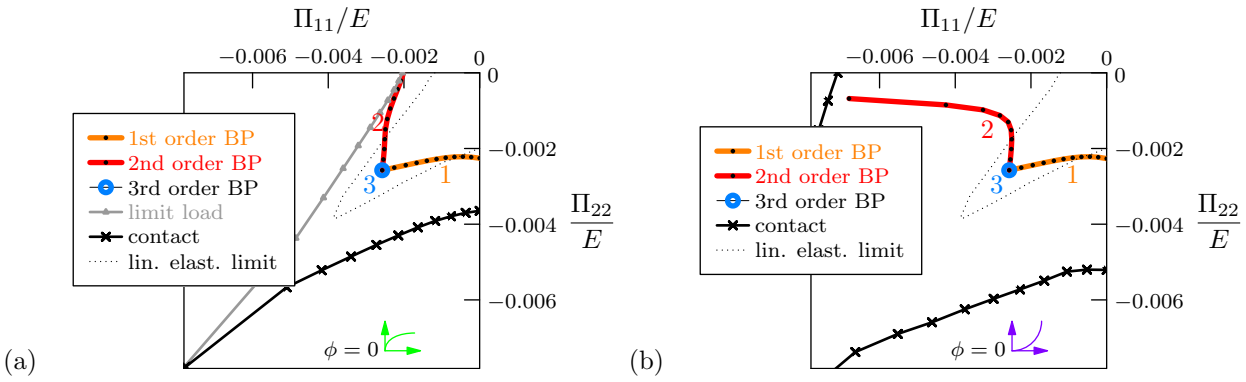


Figure 6: Onset-of-instability (bifurcation) for circular cell hexagonal honeycombs, with constitutively nonlinear cell walls under biaxial in-plane loading aligned with the axes of orthotropy ($\phi = 0$) for (a) softening material and (b) stiffening material.

Results for the case of constitutively nonlinear cell walls under loading aligned with the axes of orthotropy ($\phi = 0$) are given in Figure 6. The graph in Figure 6(a) corresponds to a softening material, and the graph in Figure 6(b) corresponds to a hardening material. Note that for the softening material case in Figure 6(a), the paths with $|\Pi_{11}| > |\Pi_{22}|$ result in a maximum load before cell wall contact, whereas the contrary is observed along paths with $|\Pi_{11}| < |\Pi_{22}|$. For the hardening material case in Figure 6(b), the behavior changes dramatically for paths with $|\Pi_{11}| > |\Pi_{22}|$ with cell contact occurring before maximum load and where a wider range of loading paths about $\theta = 0$ remains stable all the way to cell contact.

The curves in Figure 7 summarize the previous results by presenting the comparison of the onset-of-instability (bifurcation) curves for the three types of constitutive behavior. The constitutive non-linearity of the cell wall material affects only radial loading paths where $|\Pi_{11}| > |\Pi_{22}|$ ($0 < \theta < \pi/4$), in as much as the first (always double) bifurcation along the loading path occurs in the nonlinear regime of the principal solution. As expected, increasing the cell wall stiffness increases the critical load corresponding to the first bifurcation along each path and also enlarges the stable zone about the uniaxial compression along the X_1 direction, i.e. the radial sector where no bifurcation can be found. In the remaining radial loading paths with $|\Pi_{11}| < |\Pi_{22}|$ ($\pi/2 \geq \theta > \pi/4$) the first (always simple) bifurcation occurs mostly within the linear regime of the principal solution or just immediately afterwards, and hence the corresponding onset-of-instability curves remain almost identical for the three constitutive laws considered here.

4.2.2. Primary Bifurcation Solutions for Different Loading Paths and Associated Supercells

The post-bifurcation behavior of linearly elastic circular cell hexagonal honeycombs loaded along the axes of orthotropy ($\phi = 0$) is presented in this section for three loading paths: (i) the uniaxial compressive loading path in direction X_2, i.e. $\theta = \pi/2$, where a simple bifurcation point destabilizes the corresponding

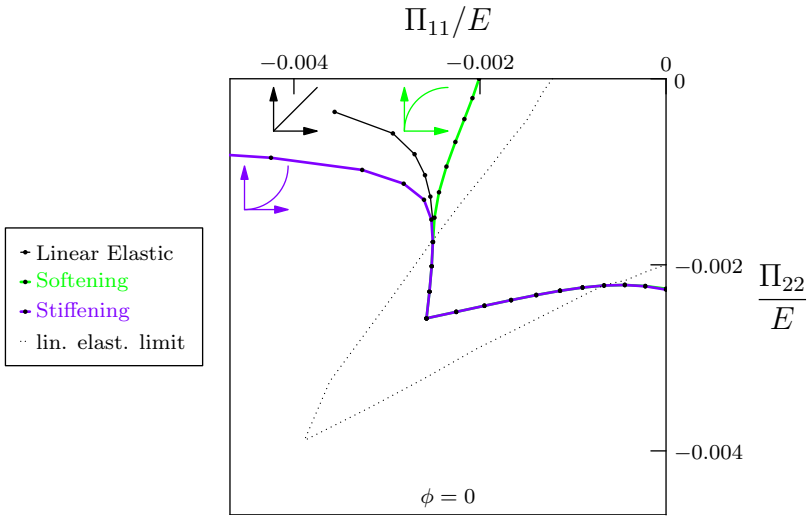


Figure 7: Comparison of onset-of-instability (bifurcation) curves for circular cell hexagonal honeycombs with different constitutive laws: linear elastic ($m = 1$, solid black line), softening ($m = 0.9$, solid green line) and stiffening ($m = 2$, solid purple line) under biaxial in-plane loading aligned with the axes of orthotropy ($\phi = 0$). The V-shaped region in stress space where the principal solution is in the linearly elastic regime is also indicated by dotted lines.

loading path; (ii) the loading path with $\theta = \tan^{-1}(0.4)$, where a double bifurcation point destabilizes the corresponding loading path; and (iii) the equibiaxial compression path with $\theta = \pi/4$ where a triple bifurcation point destabilizes the corresponding loading path. The non-existence of a bifurcation instability before the first occurrence of cell wall contact for uniaxial compression along X_1 is the reason for choosing a loading path angle $\theta = \tan^{-1}(0.4)$. These three characteristic loading paths provide a representative example for each possible post-bifurcation behavior.

(i) Uniaxial compression in direction X_2 ($\theta = \pi/2$)

On the radial loading path corresponding to a uniaxial compression along X_2 (i.e. $\theta = \pi/2,\ \phi = 0$), the first instability encountered corresponds to a simple bifurcation at $(1 - U_{22}, \lambda) = (0.0495,\ 2.3\ 10^{-3})$. As seen from Figure 8(b) this bifurcation is associated to dimensionless wavenumbers $(k_1, k_2) = (\pm 0.5, \pm 0.5)$ [11]. The corresponding eigenmodes involve a unit cell of the type presented in Figure 8(a), which is composed of two primitive unit cells. The symmetry group G of the energy $\mathcal{E}$ defined on this unit cell takes into account the symmetry of the geometry and loading and has the following generators: clockwise rotation by π (C_2), mirror symmetry (σ_1) with respect to an horizontal axis situated at a quarter height of the unit cell (see Figure 8(a)) and the internal translational symmetry along $\mathbf{G}_2$ ($T_{\mathbf{G}_2}$). Thus, the symmetry group G has 8 elements. Its irreps have maximum dimension one and hence all the bifurcations are simple.

[11] The existence of four simultaneous critical $\mathbf{k}$ vectors can be understood if one accounts for the point symmetry of the principal path and recalls that, due to the existence of an energy, $\beta_{min}(\lambda; -\mathbf{k}) = \beta_{min}(\lambda; \mathbf{k})$.

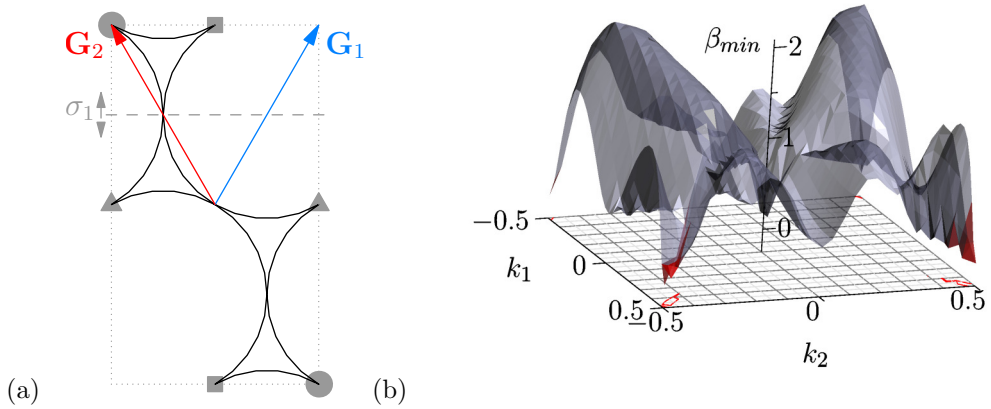


Figure 8: (a) Unit cell, identified by the Bloch-wave analysis, used for the post-bifurcation calculations for paths emerging from simple bifurcation points (loading paths $\pi/4 < \theta \leq \pi/2$). Similar symbols on boundary nodes indicate nodes linked by periodicity conditions. The position of the mirror symmetry axis of σ_1 is indicated by a dashed grey line. (b) The surface $\beta_{min}(\lambda_b^+, k_1, k_2)$ defined in (2.16) is plotted for a load (λ_b^+) slightly higher than the bifurcation load, along the path of uniaxial compression in direction X_2. Regions of negative β_{min} values highlighted in red. This figure is activatable on click to let the reader rotate it with its mouse.

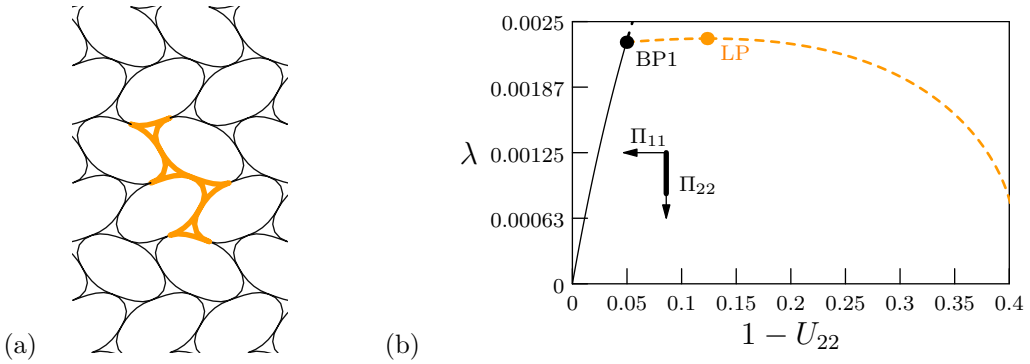


Figure 9: (a) Post-bifurcation equilibrium orbit associated with the simple bifurcation point corresponding to uniaxial compression along X_2-direction in a circular cell hexagonal honeycomb with constitutively linear cell walls. This pattern has been constructed by periodicity from the yellow colored deformed unit cell. (b) Corresponding load-strain curve. The principal path is plotted in black and the bifurcated branch in yellow. Solid line segments indicate stability with respect to the Bloch-wave criteria $\beta_{min}(\lambda, \mathbf{k}) > 0$ (see (2.16)), while dashed line segments indicate instability.

The first bifurcation encountered along this loading path is simple and symmetric (pitchfork), i.e. $\lambda_1 = 0$, $\mathcal{E}_{11\lambda} = -1$, $\mathcal{E}_{111} = 0$, $\mathcal{E}_{1111} \neq 0$ (see (2.20), (2.21)) and the post-bifurcated path is found by following the unique eigenvector of the tangent stiffness matrix. A representative path of the unique post-bifurcated orbit is depicted in Figure 9(a) and it has a symmetry group generated only by the clockwise π rotation (C_2).

The load-strain curve for this post-bifurcated orbit is depicted, along with the corresponding curve for the principal path, in Figure 9(b); the bifurcated path is calculated up to first contact of the cell walls.

Bloch-wave analysis applied on the bifurcated path in Figure 9(b) using the unit cell of Figure 8(a), finds it to be unstable. The instability is due to long wavelengths (for $k_i \ll 1$) and starts immediately at the bifurcation point, marked by a black circle labeled "BP1". This primary path becomes unstable with respect to smaller, finite wavelength perturbations, as its bifurcation amplitude increases. The path reaches a limit point at $(1-U_{22}, \lambda) = (0.13476,\ 2.34\ 10^{-3})$, represented by a yellow circle labeled "LP" on Figure 9(b).

(ii) Biaxial compression ($\theta = \tan^{-1}(0.4)$)

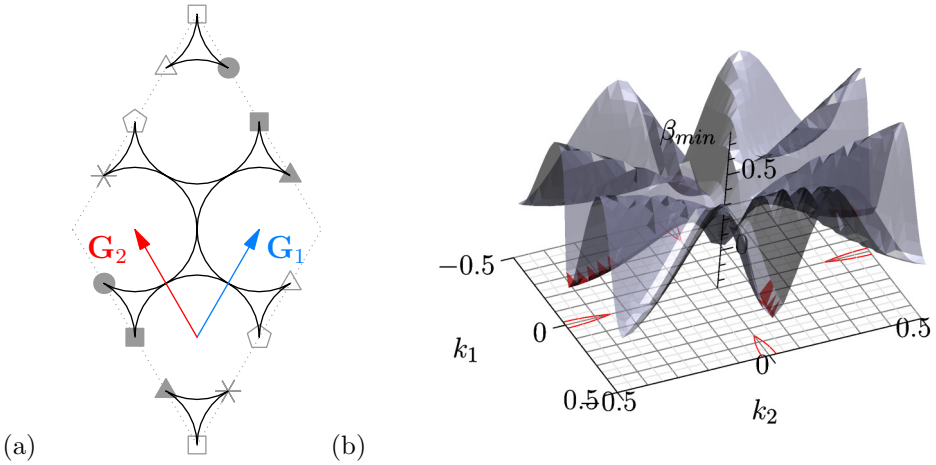


Figure 10: (a) Unit cell identified by the Bloch-wave analysis used for the post-bifurcation calculations for paths emerging from double bifurcation points (load paths $0 < \theta < \pi/4$). Similar symbols on boundary nodes indicate nodes linked by periodicity conditions. (b) The surface $\beta_{min}(\lambda_b^+, k_1, k_2)$ defined in (2.16) is plotted for a load (λ_b^+) slightly higher than the bifurcation load, along a loading path $\theta = \tan^{-1}(0.4)$. Regions of negative β_{min} values highlighted in red. This figure is activatable on click to let the reader rotate it with its mouse.

On the radial loading path corresponding to a biaxial compression aligned with the principal axes (i.e. $\theta = \tan^{-1}(0.4),\ \phi = 0$), the first instability encountered corresponds to a double bifurcation at the point $(1-U_{11}, 1-U_{22}, \lambda) = (0.067,\ -0.037,\ 2.62\ 10^{-3})$. As seen from Figure 10(b) this bifurcation is associated to dimensionless wavenumbers $(k_1, k_2) = (\pm 0.5, 0)$ and $(k_1, k_2) = (0, \pm 0.5)$. The corresponding eigenmodes involve a unit cell of the type presented in Figure 10(a), which is composed of four primitive unit cells. The symmetry group G of the energy $\mathcal{E}$ defined on this unit cell takes into account the symmetry of the geometry and loading and has the following generators: clockwise rotation by π (C_2), mirror symmetry with respect to a horizontal axis situated at the center of the unit cell (σ_1) and the internal translational symmetries along $\mathbf{G}_1$ ($T_{\mathbf{G}_1}$) and $\mathbf{G}_2$ ($T_{\mathbf{G}_2}$). Thus, the symmetry group G has a total of 16 elements and its irreps have maximum dimension two.

The first bifurcation encountered along this loading path is double and symmetric (pitchfork), i.e. $\lambda_1 = 0,\ \mathcal{E}_{ijk} = 0$ (see (2.20)). Consequently the initial tangents of the bifurcated equilibrium paths

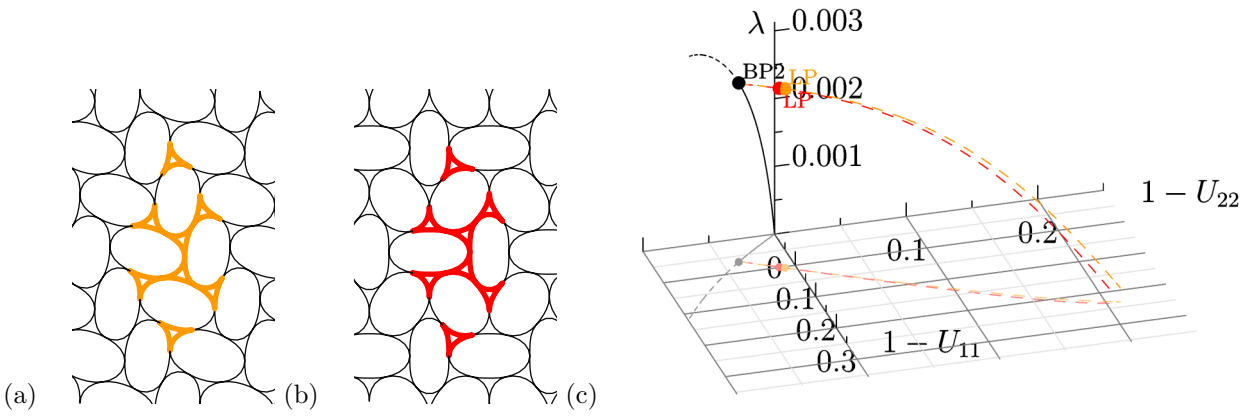


Figure 11: The two different post-bifurcation equilibrium orbits – (a) Orbit I and (b) Orbit II – associated with the double bifurcation point corresponding to biaxial compression with a loading path angle $\theta = \tan^{-1}(0.4)$ for a circular cell hexagonal honeycomb with constitutively linear cell walls. These modes have been reconstructed by periodicity from the colored deformed unit cells. (c) Corresponding load-strain curves. The principal path is plotted in black and the bifurcated orbits in yellow and red. Solid line segments indicate stability with respect to the Bloch-wave criteria $\beta_{min}(\lambda, \mathbf{k}) > 0$ (see (2.16)), while dashed line segments indicate instability. This figure is activatable on click to let the reader rotate it with its mouse.

will be found from (2.21). Using the τ^μ equivariance of the two-dimensional ($n_\mu = 2$) equilibrium equations of the system restricted on the null space $\mathcal{N}_\mu$, we find only two different non-zero coefficients $\mathcal{E}_{ijkl}$ in (2.21)

$$\mathcal{E}_{1111} = \mathcal{E}_{2222} \ , \quad \mathcal{E}_{1122} \ , \tag{4.1}$$

with the rest generated by the symmetries: $\mathcal{E}_{\pi(ijkl)} = \mathcal{E}_{ijkl}$, where $\pi(ijkl)$ is any permutation of the indices $ijkl$. Recalling $\mathcal{E}_{ij\lambda} = -\delta_{ij}$ (by appropriate normalization of the two eigenvectors $\overset{1}{u}$ and $\overset{2}{u}$), we obtain two different post-bifurcated orbits. One representative path from each orbit is characterized by

$$\begin{aligned} \text{Orbit I} \ : \quad & (\alpha_1, \alpha_2) = (1, 0) \ , \\ \text{Orbit II} \ : \quad & (\alpha_1, \alpha_2) = (1/\sqrt{2}, 1/\sqrt{2}) \ . \end{aligned} \tag{4.2}$$

These paths are shown in Figure 11: the Orbit I path (plotted in yellow), whose typical configuration is depicted in Figure 11(a), has a symmetry subgroup with generators $\{C_2, T_{\mathbf{G}_2}\}$ but no mirror symmetry and the Orbit II path (plotted in red), whose typical configuration is depicted in Figure 11(b), has a symmetry subgroup with generators $\{C_2, \sigma_1\}$ but no translational symmetry.

The load-strain curves of the principal path and the two bifurcated orbits calculated up to first contact between cell walls, are plotted in Figure 11(c). In order to properly distinguish Orbit I and Orbit II paths, the load-displacement curves are plotted in a three-dimensional space where the two horizontal axes are the strains $1 - U_{11}$ and $1 - U_{22}$ and the vertical axis is λ. Bloch-wave analysis applied on each one of the two bifurcated paths in Figure 11 using the unit cell of Figure 10(a) finds them to be both unstable. The Orbit I path reaches a maximum load turning point at $(1 - U_{11}, 1 - U_{22}, \lambda) = (0.103, \ -0.008, \ 2.64\ 10^{-3})$. Similarly,

Orbit II reaches a maximum load turning point at $(1-U_{11}, 1-U_{22}, \lambda) = (0.099,\ -0.012,\ 2.64\ 10^{-3})$.

(iii) Equibiaxial compression ($\theta = \pi/4$)

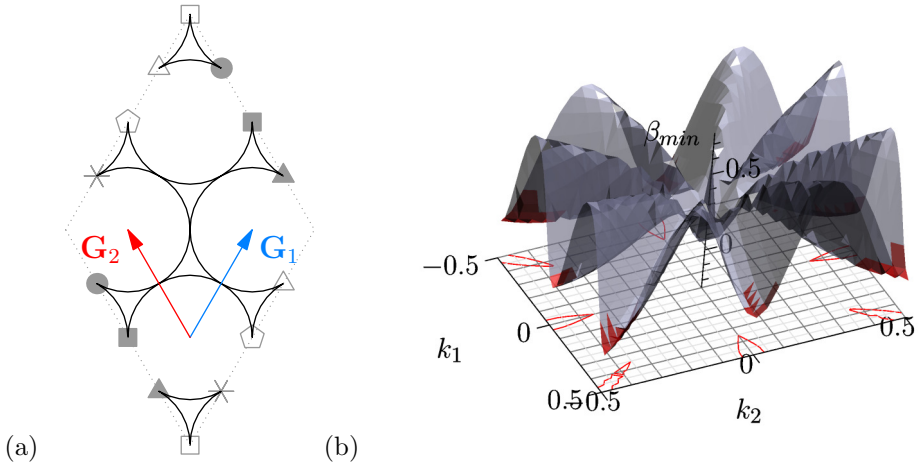


Figure 12: (a) Unit cell identified by the Bloch-wave analysis used for the post-bifurcation equilibrium paths emerging from the triple bifurcation point (load path angle $\theta = \pi/4$). Similar symbols on boundary nodes indicate nodes linked by periodicity conditions. (b) The surface $\beta_{min}(\lambda_b^+, k_1, k_2)$ defined in (2.16) is plotted for a load (λ_b^+) slightly higher than the bifurcation load, along the principal path of equibiaxial compression. Regions of negative β_{min} values highlighted in red.This figure is activatable on click to let the reader rotate it with its mouse.

On the radial loading path corresponding to an equibiaxial compression (i.e. $\theta = \pi/4,\ \phi = 0$), the first instability encountered corresponds to a triple bifurcation at $(1-U_{11}, 1-U_{22}, \lambda) = (0.0078, 0.0078, 1.84\ 10^{-3})$. As seen from Figure 12(b) this bifurcation is associated to dimensionless wavenumbers $(k_1, k_2) = (\pm 0.5, 0)$, $(k_1, k_2) = (0, \pm 0.5)$ and $(k_1, k_2) = (\pm 0.5, \pm 0.5)$. The corresponding eigenmodes involve a unit cell of the type presented in Figure 12(a), which is composed of four primitive unit cells. The symmetry group G of the energy $\mathcal{E}$ defined on this unit cell takes into account the symmetry of the geometry and loading and has the following generators: clockwise rotation by $2\pi/6$ (C_6), mirror (σ_1) and the internal translational symmetries along $\mathbf{G}_1$ ($T_{\mathbf{G}_1}$) and $\mathbf{G}_2$ ($T_{\mathbf{G}_2}$). The symmetry group G has thus a total of 48 elements and its irreps have maximum dimension three.

The first bifurcation point encountered along this path is a triple symmetric (pitchfork) one, i.e. $\lambda_1 = 0$, $\mathcal{E}_{ijk} = 0$ (see (2.20)). Consequently the initial tangents of the bifurcated equilibrium paths will be found from (2.21). Using the τ^μ equivariance of the three-dimensional ($n_\mu = 3$) equilibrium equations of the system restricted on the null space $\mathcal{N}_\mu$, we find only two different non-zero coefficients $\mathcal{E}_{ijkl}$ in (2.21)

$$\mathcal{E}_{1111} = \mathcal{E}_{2222} = \mathcal{E}_{3333}\ , \quad \mathcal{E}_{1122} = \mathcal{E}_{2233} = \mathcal{E}_{3311}\ , \tag{4.3}$$

with the rest generated by the symmetries: $\mathcal{E}_{\pi(ijkl)} = \mathcal{E}_{ijkl}$. Recalling $\mathcal{E}_{ij\lambda} = -\delta_{ij}$ (by appropriate normalization of the three eigenvectors $\overset{1}{u}$, $\overset{2}{u}$ and $\overset{3}{u}$), we obtain three different post-bifurcated orbits. One

representative path from each orbit is characterized by

$$\begin{aligned} \text{Orbit I} &: \quad (\alpha_1, \alpha_2, \alpha_3) = (1, 0, 0) \ , \\ \text{Orbit II} &: \quad (\alpha_1, \alpha_2, \alpha_3) = (1/\sqrt{2}, 1/\sqrt{2}, 0) \ , \\ \text{Orbit III} &: \quad (\alpha_1, \alpha_2, \alpha_3) = (1/\sqrt{3}, 1/\sqrt{3}, 1/\sqrt{3}) \ . \end{aligned} \tag{4.4}$$

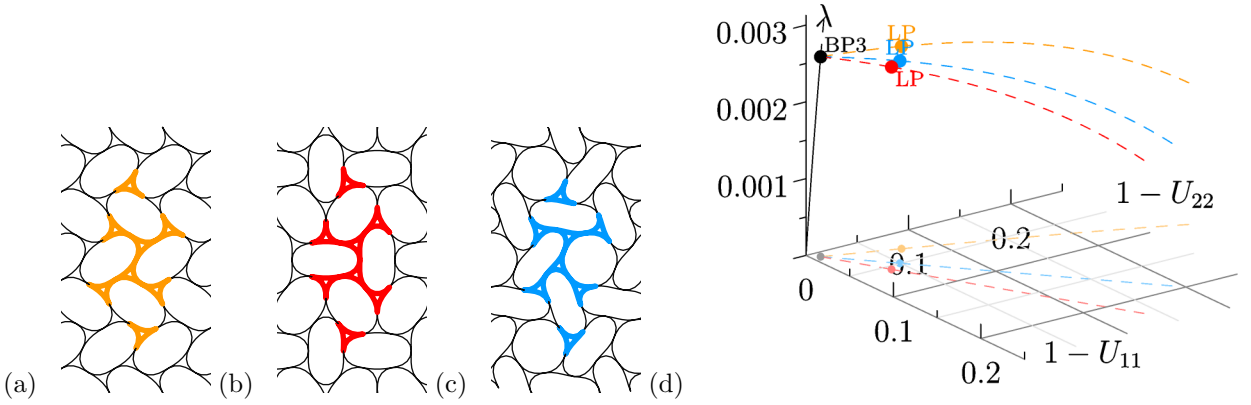


Figure 13: The three different post-bifurcation equilibrium orbits – (a) Mode I, (b) Mode II, (c) Mode III – associated with the triple bifurcation point corresponding to equibiaxial compression with a loading path angle $\theta = \pi/4$ for a circular cell hexagonal honeycomb with constitutively linear cell walls. These modes have been reconstructed by periodicity from the colored deformed unit cells. (d) Corresponding load-strain curves. The principal path is plotted in black and the bifurcated orbits in yellow, red and blue. Solid line segments indicate stability with respect to the Bloch-wave criteria $\beta_{min}(\lambda, \mathbf{k}) > 0$ (see (2.16)), while dashed line segments indicate instability. This figure is activatable on click to let the reader rotate it with its mouse.

These paths are shown in Figure 13: the Orbit I path (plotted in yellow), whose typical configuration is depicted in Figure 13(a), has a symmetry subgroup with generators $\{C_2, T_{\mathbf{G}_1+\mathbf{G}_2}, T_{\mathbf{G}_1-\mathbf{G}_2}\}$, the Orbit II path (plotted in red), whose typical configuration is depicted in Figure 13(b), has a symmetry subgroup with generators $\{C_2, \sigma_1\}$ and the Orbit III path (plotted in blue), whose typical configuration is depicted in Figure 13(c), has a symmetry subgroup with generator $\{C_6\}$. Notice that the paths corresponding to the last two orbits have no translational symmetry.

The load-strain curves of the principal path and the three bifurcated orbits calculated up to first contact between cell walls, are plotted in Figure 13(d). In order to properly distinguish Orbit I, Orbit II and Orbit III paths, the load-strain curves are plotted in a three-dimensional space where the two horizontal axes are the strains $1-U_{11}$ and $1-U_{22}$ and the vertical axis is λ. Notice that Orbit I and Orbit II paths involve different macroscopic strains $1-U_{11} \neq 1-U_{22}$ while Orbit III paths have equal macroscopic strains $1-U_{11} = 1-U_{22}$, as seen from their projections in the graph of Figure 13(d).

Bloch-wave analysis is applied to each one of the three bifurcated paths in Figure 13 using the unit cell of Figure 12(a) and finds them to be all unstable, reaching a maximum load and subsequently evolving under a monotonically decreasing load. Orbit I path reaches a maximum load (turning) point at point

$(1-U_{11}, 1-U_{22}, \lambda) = (0.027,\ 0.070,\ 2.64\ 10^{-3})$. Orbit II reaches a maximum load (turning) point at $(1-U_{11}, 1-U_{22}, \lambda) = (0.058,\ 0.037,\ 2.635\ 10^{-3})$. Similarly, Orbit III reaches a maximum load (turning) point at $(1-U_{11}, 1-U_{22}, \lambda) = (0.048,\ 0.048,\ 2.635\ 10^{-3})$.

The orbit with the lowest energy is Orbit III which reaches a maximum load shortly after the onset of bifurcation and is unstable only for very large wavelengths (see further, Combescure et al. (2016)), explaining its appearance in the finite specimen experiments of Papka and Kyriakides (1999a).

4.3. Square Honeycomb

4.3.1. Principal Paths and Onset-of-Instability Based on the Primitive Cell

The onset-of-instability curves computed for the loading defined in (2.1), plotted in macroscopic stress space for the circular cell square honeycomb are shown in Figure 14(a) for the case of loading aligned with the axes of orthotropy $\phi = 0$ and in Figure 14(b) for the case of loading at $\phi = \pi/15$ with respect to the orthotropy axes. Onset-of-instability curves are plotted in solid lines, curves indicating the onset of cell contact are plotted in lines with cross markers.

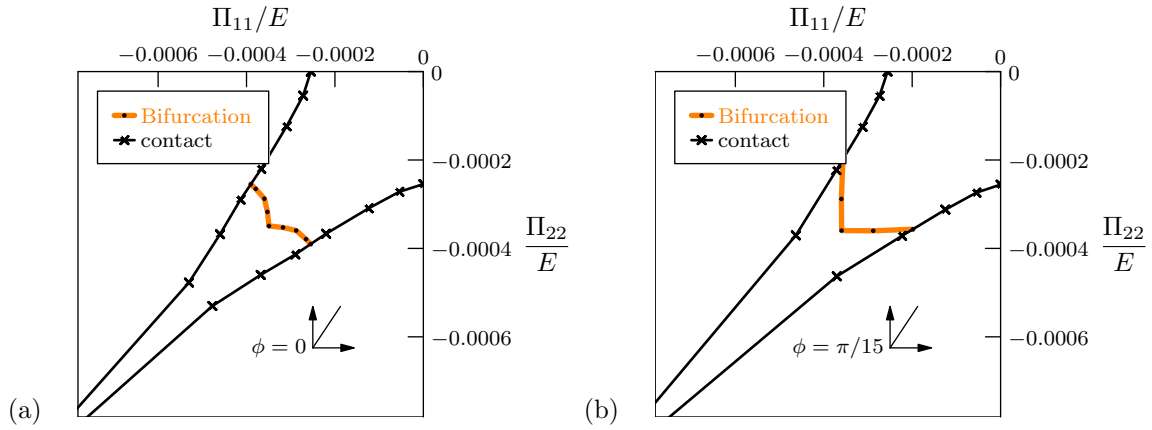


Figure 14: Onset-of-instability (bifurcation) for circular cell square honeycombs, with linearly elastic cell walls under biaxial in-plane loading (a) aligned with the axes of orthotropy ($\phi = 0$) and (b) rotated with respect to the axes of orthotropy ($\phi = \pi/15$). First bifurcation along any loading path always corresponds to global modes (long wavelength modes $k_i \to 0$).

The results shown here correspond to linear elastic cell walls, since the constitutive law is found to play an insignificant role in the stability results (calculations not shown here). Only a small range of path angles near the equibiaxial loading ($\theta = \pi/4$) lead to an instability prior to contact between cell walls. Moreover, all instabilities occur at an infinitely long wavelength ($k_i \to 0$). These results are consistent with Ohno et al. (2004); Haghpanah et al. (2014) but puzzling, since the continuum case of biaxially compressed periodic, porous elastomers with the same symmetry shows local bifurcation modes (Michel et al., 2007; Bertoldi et al., 2008).

Some explanation for these results could be found in the work by Overvelde et al. (2012); Overvelde and Bertoldi (2014) that shows the important role played by the shape of the pore in porous elastomers on the length scale of bifurcations. In particular, a change in the pore geometry may result in a switch from microscopic to macroscopic buckling. Moreover, recent work by He et al. (2018) underlines the influence of the stiffness of the joints in square grid lattices. The difference between our present results and those for porous elastomers may be explained by the fact that a structural shell model is used for the cell walls and that this model reaches its limits of validity when cell walls become thick. Further, the shell model may provide an inadequate representation of the joint behavior. Such issues with the structural shell model have already been reported in Combescure et al. (2016) where it was noticed that a shell model under dead load control leads to zero energy modes that artificially create a triple bifurcation point when a two-dimensional plane strain model of the same problem finds separate simple and double bifurcation points.

5. Conclusions

Of interest in this work are the deformation patterns and their stability of finitely strained circular cell honeycombs. We consider two different geometric arrangements, hexagonal and square, biaxial compression along loading paths either aligned or at an angle with respect to the axes of orthotropy, and different constitutive laws for the cell walls which can undergo arbitrarily large rotations. Given the high degree of symmetry of these infinite structures, the introduction of numerical imperfections is inadequate for the study of their behavior past the onset of first bifurcation. Consequently group theory considerations are further developed to efficiently calculate all the different post-bifurcated equilibrium orbits and their stability.

Using Bloch wave analysis, it is found that the hexagonal honeycombs of infinite extent have a first bifurcation corresponding to a local mode (involving a finite number of primitive cells). By redefining the problem on an appropriate supercell and finding its corresponding symmetry group, we calculate the post-bifurcated orbits and their stability. Depending on load path orientation, the first bifurcation encountered along a loading path can be simple, double or even triple. Cell wall constitutive response is found to strongly influence the onset of double bifurcations but leaves the simple ones, as well as the triple, unchanged. Rotation of the principal stress axes with respect to the axes of orthotropy results in simple bifurcations insensitive to the constitutive response, save for a triple bifurcation at equibiaxial compression which is independent of the principal axes rotation.

In following the different bifurcated orbits, we found that they all show a maximum load shortly after their emergence from the principal path. Moreover, Bloch wave analysis shows that they are always unstable, indicating the impossibility of their observation in large enough laboratory specimens. However some orbits stabilize for wavenumbers larger than a small critical value (corresponding to large but finite wavelengths), thus explaining their observation in laboratory experiments. Bloch wave analysis for circular cell square

honeycombs gives the first bifurcation along any loading path corresponding to a global mode ($\mathbf{k} \to \mathbf{0}$). Consequently there is no point in following bifurcated equilibrium paths since they depend on specimen size and boundary conditions. Further study of the circular cell square honeycombs using a two-dimensional plane strain formulation (as opposed to the current shell element formulation) is necessary to elucidate the change in behavior of continuum porous elastomers as the volume fraction goes to zero.

The group-theoretic approach developed and described in Section 2.3 to investigate the deformation patterns and their stability in finitely strained periodic honeycombs is a consistent and general methodology that finds the bifurcating equilibrium paths in these high-symmetry structures. The circular cell honeycomb application studied here investigates a large range of (compressive) loading paths and explains the observation of deformation patterns observed experimentally. It can be used to study nonlinear periodic composites with arbitrary microstructures, a class of engineering materials with an ever-growing range of applications.

ACKNOWLEDGMENTS

The work of C. C. was supported by The Aerospace Engineering and Mechanics Department of the University of Minnesota through NSF grants PHY-0941493 and CMMI-1462826 and the LMS at the Ecole Polytechnique during two consecutive, one-year post-doctoral fellowships in each Institution. The work of R. E. was supported by the NSF grants PHY-0941493 and CMMI-1462826 and by the LMS during several short visits. The authors acknowledge the Minnesota Supercomputing Institute (MSI) at the University of Minnesota for providing resources that contributed to the research results reported within this work. http://www.msi.umn.edu.

6. References

Bertoldi, K., Boyce, M., Deschanel, S., Prange, S., Mullin, T., 2008. Mechanics of deformation-triggered pattern transformations and superelastic behavior in periodic elastomeric structures. J. Mech. Phys. Solids 56, 2642–2668.

Combescure, C.J., Henry, P., Elliott, R.S., 2016. Post-bifurcation and stability of a finitely strained hexagonal honeycomb subjected to equi-biaxial in-plane loading. International Journal of Solids and Structures 88, 296–318.

Elliott, R.S., Shaw, J.A., Triantafyllidis, N., 2006. Stability of crystalline solids—II: Application to temperature-induced martensitic phase transformations in bi-atomic crystals. Journal of the Mechanics and Physics of Solids 54, 193–232.

Elliott, R.S., Triantafyllidis, N., Shaw, J.A., 2011. Reversible stress-induced martensitic phase transformations in a bi-atomic crystal. Journal of the Mechanics and Physics of Solids 59, 216–236.

Golublitsky, M., Stewart, I., Schaeffer, D.G., 1988. Singularities and Groups in Bifurcation Theory. volume 2 of *Applied Mathematical Sciences*. Springer-Verlag.

Haghpanah, B., Papadopoulos, J., Mousanezhad, D., Nayeb-Hashemi, H., Vaziri, A., 2014. Buckling of regular, chiral and hierarchical honeycombs under a general macroscopic stress state. Proc. R. Soc. A Math. Phys. Eng. Sci. 470, 20130856–20130856.

He, Y., Zhou, Y., Liu, Z., Liew, K.M., 2018. Buckling and pattern transformation of modified periodic lattice structures. Extrem. Mech. Lett. 22, 112–121.

Hutchinson, J.W., 1974. Plastic buckling. Advances in Applied Mechanics 14, 66–143.

Karagiozova, D., Yu, T., 2008. Strain localization in circular honeycombs under in-plane biaxial quasi-static and low-velocity impact loading. Int. J. Impact Eng. 35, 753–770.

McWeeny, R., 2002. Symmetry: An introduction to group theory and its applications. Courier Dover Publications.

Michel, J.C., Lopez-Pamies, O., Ponte Castañeda, P., Triantafyllidis, N., 2007. Microscopic and macroscopic instabilities in finitely strained porous elastomers. Journal of the Mechanics and Physics of Solids 55.

Ohno, N., Okumura, D., Niikawa, T., 2004. Long-wave buckling of elastic square honeycombs subject to in-plane biaxial compression. Int. J. Mech. Sci. 46, 1697–1713.

Okumura, D., Ohno, N., Noguchi, H., 2002. Post-buckling analysis of elastic honeycombs subject to in-plane biaxial compression. International journal of solids and structures 39, 3487–3503.

Overvelde, J.T., Shan, S., Bertoldi, K., 2012. Compaction through buckling in 2D periodic, soft and porous structures: Effect of pore shape. Adv. Mater. 24, 2337–2342.

Overvelde, J.T.B., Bertoldi, K., 2014. Relating pore shape to the non-linear response of periodic elastomeric structures. J. Mech. Phys. Solids 64, 351–366.

Papka, S., Kyriakides, S., 1999a. Biaxial crushing of honeycombs:—part 1: Experiments. International Journal of Solids and Structures 36, 4367–4396.

Papka, S., Kyriakides, S., 1999b. In-plane biaxial crushing of honeycombs?: Part ii: Analysis. International Journal of Solids and Structures 36, 4397–4423.

Saiki, I., Ikeda, K., Murota, K., 2005. Flower patterns appearing on a honeycomb structure and their bifurcation mechanism. International Journal of Bifurcation and Chaos 15, 497–515.

Sorkin, V., Elliott, R.S., Tadmor, E.B., 2014. A local quasicontinuum method for 3d multilattice crystalline materials: Application to shape-memory alloys. Modelling and Simulation in Materials Science and Engineering 22, 055001.

Surjadi, J.U., Gao, L., Du, H., Li, X., Xiong, X., Fang, N.X., Lu, Y., 2019. Mechanical metamaterials and their engineering applications. Adv. Eng. Mater. 21, 1800864 (1–37).

Triantafyllidis, N., Peek, R., 1992. On stability and the worst imperfection shape in solids with nearly simultaneous eigenmodes. International Journal of Solids and Structures 29, 2281 – 2299.

Triantafyllidis, N., Samanta, S.K., 1986. Bending effects on flow localization in metallic sheets. Proceedings of the Royal Society of London A: Mathematical, Physical and Engineering Sciences 406, 205–226. http://rspa.royalsocietypublishing.org/content/406/1831/205.full.pdf.

Triantafyllidis, N., Schraad, M., 1998. Onset of failure in aluminum honeycombs under general in-plane loading. Journal of the Mechanics and Physics of Solids 46, 1089–1124.